doi.org/10.1002/batt.202000054



# Compositional Effects of Gel Polymer Electrolyte and Battery Design for Zinc-Air Batteries

Thuy Nguyen Thanh Tran,[a] Drew Aasen,[a] Dinara Zhalmuratova,[a] Matthew Labbe,[a] Hyun-Joong Chung,[a] and Douglas G. Ivey*[a]

Poly(acrylic acid) (PAA) is a promising polymer host to support alkaline electrolytes in Zn-air batteries. Herein, precursors containing different concentrations of monomers, crosslinkers and additives such as zinc oxide in alkaline solution are polymerized to fabricate gel polymer electrolytes (GPEs) via one-pot synthesis. The compositional effects of the GPEs on battery performance are evaluated and a more efficient cell design is demonstrated. With a vertical double air electrode configuration, ZABs using PAA-based electrolytes show unprecedented performance including high specific energy (913 Wh $kg_{Zn}^{-1}$), excellent cycling stability (at least 160 cycles at $2\times10$ mA $cm^{-2}$) and high power density output ($2\times$ 135 mW $cm^{-2}$). The study represents a viable option to replace aqueous electrolytes for high performing ZABs.

## 1. Introduction

Compared to other batteries and capacitors, Zn-air batteries (ZABs) offer several advantages, e.g., safety, low cost and high specific energy density (1218 Wh $kg^{-1}$).[1] To avoid complexities in the construction of flexible batteries, gel polymer electrolytes (GPEs) are used to contain alkaline, aqueous solutions in a polymer host. As alternatives to aqueous electrolytes, GPEs prevent flooding of the air electrode and leakage concerns associated with liquid electrolytes, inhibit dendrite formation on the Zn electrode and reduce carbonation at the air electrode. In fact, GPEs are widely employed in energy storage devices because they are safe and flexible, making them adaptable to various designs; some can be engineered to be thermally responsive or self-healing.[2–3]

The popular choices for the polymer host include poly (ethylene oxide) (PEO), poly(vinyl alcohol) (PVA), polyacrylamide, cellulose, gelatin and poly(acrylic acid) (PAA), as well as dual-network gels that are based on these polymers.[4–11] Since 2002, PVA–KOH has become the alkaline GPE of choice with an ionic conductivity in the range of 1–100 mS $cm^{-1}$; conductivity depends on electrolyte content and concentration in the GPE.[12–16] On the other hand, PAA–KOH has a much higher conductivity (200–460 mS $cm^{-1}$) due to its hydrophilicity and can be fabricated via one-pot synthesis since acrylic acid monomers are miscible with highly concentrated KOH, which eliminates a need for solvent-casting or dialyzing processes.[17] Most research work up to now has focused on utilizing PAA-based GPEs' mechanical durability for flexible[18–20] and stretchable ZAB applications.[9] To the best of our knowledge, PAA–KOH composition has previously been optimized solely based on ionic conductivity for primary Al-air batteries.[21] The optimized product contained ~8.2 M of KOH, 1 M of PAA and 74 mM of crosslinker before percolation. For rechargeable applications, the effects of gel composition, including additives, and gel mechanical properties on battery performance require further investigation.

KOH provides the electrolytic ion species to GPEs and additives can be incorporated in GPEs to improve the cycle life of ZABs. Zinc compounds, such as zinc chloride ($ZnCl_2$), zinc oxide (ZnO) or zinc acetate ($Zn(Ac)_2$), are reported to generate zincate ions and act as a corrosion inhibitor.[22–24] These materials can be incorporated in the Zn electrode or mixed in the electrolyte. Park et al. reported that ZnO is the most soluble substance of the three compounds in alkaline solutions. Thus, after the first charging process, the highest discharge capacities were obtained from a Zn anode with ZnO. Additionally, since more zincate ions were generated, better reversibility of the zincate ions during charging was achieved for ZnO compared with the other zinc compounds.[24] On the other hand, several reports use aqueous alkaline electrolytes that are pre-saturated with ZnO powder (~0.6 M).[25–29] The optimal amount of ZnO appears not to have been identified; e.g., Gaikwad et al. prepared PAA in saturated ZnO,[30] while some others do not use any additives.[10] Although ZnO is considered to be helpful for the oxygen evolution reaction (OER), excessive amounts of ZnO may reduce the conductivity of GPEs and trigger early passivation. Therefore, identifying an optimized amount of ZnO in PAA–KOH gel is needed.

Even though Li-ion batteries (LIBs) are commercially available for electric vehicles (EVs) with a full charge range from 200 to 400 km, their energy density is not entirely adequate for EVs. Compared with ZABs, LIBs have a lower theoretical specific energy (260 Wh $kg^{-1}$).[31] The capacity of LIBs for current EVs, such as the Renault Twizzy, Hyundai Ioniq, Nissan Leaf and VW E-Golf, often range from 6 to 30 kWh.[32] Targets set by the

[a] T. N. T. Tran, D. Aasen, D. Zhalmuratova, M. Labbe, Prof. H.-J. Chung, Prof. D. G. Ivey
Department of Chemical and Materials Engineering
Faculty of Engineering, University of Alberta
Edmonton, Alberta, Canada T6G 1H9
E-mail: divey@ualberta.ca

Supporting information for this article is available on the WWW under https://doi.org/10.1002/batt.202000054

United States Advanced Battery Consortium LLC for EVs require power supply voltages of 220 V–420 V with usable energy of 45 kWh.[33] From a practical point of view, however, it is very challenging to obtain an efficient electrically rechargeable ZAB. This involves a stack consisting of hundreds of ZAB cells in series to raise the voltage to the required level. However, ZABs can act as a range extender in conjunction with a LiB pack. Solid-state ZABs, which are cheaper than LIBs and more resilient against shock, vibration and high temperature than aqueous ZABs, can provide a compact, lower power, continuous discharging source for EVs and home grid energy storage.[34–35] A conventional ZAB which is constructed in a planar arrangement where one Zn electrode is paired with one air electrode has a theoretical open circuit voltage of ~1.6 V. In our previous study, tri-electrode ZABs with PAA showed promising performance in terms of cycling stability.[36] However, in a commercial battery pack, a tri-electrode design would be complex. On the other hand, an alternative to a tri-electrode cell design is a configuration with two bifunctional air electrodes located on either side of the Zn electrode. This design increases the air electrode area without significantly increasing the cell volume, which helps to enhance the specific power of a ZAB considerably. This single cell design is made more feasible when employing GPEs, since the solid nature and hydrophilicity of the polymer network can prevent leakage issues associated with liquid electrolytes.

In this study, two inevitable issues that secondary ZABs experience during operation are addressed: (1) There is an increase in volume and pressure during the oxygen reduction reaction (ORR) and (2) oxygen bubbles are released during OER. Herein, we hypothesize that stiffness and stickiness of a GPE are particularly important to a rechargeable ZAB; e.g., a weaker GPE can undergo deformation to accommodate the volume change of the battery and a less adhesive GPE on the air electrode allows space for oxygen bubbles to coalesce and escape. Therefore, the first objective of this study is to address the effects of the physical properties of GPEs on battery performance by varying the concentrations of monomers and crosslinkers. The second objective is to find an optimized amount of Zn compound (either ZnO or $Zn(Ac)_2$) as an additive in GPEs. Finally, a complete comparison of cell configurations is demonstrated. A PAA-based GPE is chosen because of its availability, safety and facile fabrication, which involves one-step polymerization of monomers in an alkaline KOH precursor solution. In this sense, this paper stands as a starting point for the study of GPEs in solid-state rechargeable ZABs in grid energy storage devices and EV applications.

## Experimental Section

### Synthesis of catalysts

All chemicals were of analytical grade and used as received without further purification. Iron(II) sulfate ($FeSO_4 \cdot 7H_2O$), cobalt(II) acetate ($Co(CH_3COO)_2 \cdot 4H_2O$), sodium hydroxide (NaOH) and ethanol were obtained from Fisher. Nafion (5% w/w in water and 1-propanol) was obtained from Alfa Aesar. Nitrogen-doped multiwalled carbon nanotubes (N-CNTs) (30–50 nm diameter, 1–2 μm length) were obtained from MKnano. The gas diffusion layer (GDL) (Teflon-coated porous carbon paper, Sigracet 39 BB) was obtained from the Fuel Cell Store. Deionized water (DIW) was used to rinse and prepare all aqueous solutions.

GDL impregnated with $(Co,Fe)_3O_4$ decorated N-CNTs was utilized as the bifunctional air electrode; details regarding fabrication and characterization of the catalysts can be found in the literature.[37] Briefly, N-CNTs (50 mg), $FeSO_4 \cdot 7H_2O$ (175 mg), $Co(CH_3COO)_2 \cdot 4H_2O$ (35 mg) and NaOH (80 mg) were stirred in 10 mL of ethanol at 800 RPM for 10 min. The suspension was sonicated for 5 h and then Nafion (1 mL) and ethanol (15 mL) were added to the catalyst suspension. To prepare air electrodes, the GDL was sectioned into 4.5-cm-diameter circles and soaked in the catalyst suspension for 20 min under sonication. Afterwards, 5 mL of the catalyst suspension was vacuum filtered through each substrate. The GDL pieces were annealed at 300 °C for 30 min. The mass loading of catalysts on the GDL was ~2.5 mg $cm^{-2}$.[37]

### Synthesis of hydrogel electrolyte

PAA–KOH was used as the hydrogel electrolyte in this work. Acrylic acid (AA) (containing 200 ppm mequinol as an inhibitor), *N,N'*-methylenebis(acrylamide) (MBAA) and potassium persulfate (KPS) were obtained from Sigma-Aldrich, while solid potassium hydroxide (KOH), zinc oxide (ZnO) and zinc acetate ($Zn(Ac)_2$) were obtained from Fisher. PAA–KOH was prepared by mixing the AA monomer, MBAA crosslinker and KPS thermoinitiator in a KOH solution with varying concentrations, as shown in Table 1. The solutions were mixed using a vortexer. The electrolyte solutions were kept in an oven at 60 °C for 1 h to carry out polymerization and then allowed to cool overnight to room temperature. The concentration of KPS was fixed at 1.5 mM, which is consistent with our previous studies.[36,38] Different concentrations of PAA were utilized, i.e., 0.25, 0.5, 1, 1.5 and 2 M, and the KOH concentration was increased accordingly to ensure there was at least 6 M KOH in the PAA–KOH network. The samples are denoted as P–K1, P–K2, P–K3, P–K4 and P–K5, respectively. The crosslinker amount was adjusted to the minimum value for the PAA–KOH samples to exhibit gel-like structural consistency. For P–K1, the minimum crosslinker amount to prepare a gel-like sample could not be identified, since a gel-like consistency was not observed even when the MBAA concentration reached the solubility limit (Table S1, Figure S1).

The concentration of ZnO or $Zn(Ac)_2$ in the PAA–KOH electrolyte was also varied; i.e., 0, 0.1, 0.25, 0.4 and 0.5 M, in order to evaluate their effect on ZAB performance. The different concentrations of the additives were added separately until the gel color turned opaque, indicating the supersaturation of ZnO or $Zn(Ac)_2$ (Figure S2).

**Table 1.** Compositions of PAA–KOH samples.

| Sample | KOH [M] | PAA [M] | MBAA [mM] | KPS [mM] | Final state |
|---|---|---|---|---|---|
| P–K1 | 6.25 | 0.25 | 130[a] | 1.5 | Liquid-like |
| P–K2 | 6.5 | 0.5 | 30 | 1.5 | Gel-like |
| P–K3 | 7 | 1 | 7 | 1.5 | Gel-like |
| P–K4 | 7.5 | 1.5 | 5 | 1.5 | Gel-like |
| P–K5 | 8 | 2 | 3 | 1.5 | Gel-like |

[a] Solubility limit.

### Cell fabrication

Two designs for bi-electrode ZABs were fabricated and are shown in Figure 1. In general, a ZAB using PAA–KOH as the electrolyte can be fabricated as stacked layers using acrylic sheets as the battery casing. A conventional design is shown in Figure 1a in which one air electrode is positioned on top with one Zn electrode below. Most experiments in this work were conducted using this cell. To exploit the benefits of the solid hydrogel electrolyte, a double air electrode design was used and compared with the single air electrode design (Figure 1b). In the double air electrode design, the Zn electrode is sandwiched between two bifunctional air electrodes. The contact area between the air electrode and the electrolyte was controlled (1 $cm^2$ each side) and the thickness of the Zn sheet was 0.2 mm. The GPE thickness was 3 mm.

### Materials characterization

Conductivities of aqueous electrolyte solutions were measured with a conductivity probe (Mettler Toledo InLab 731-ISM). Conductivities of PAA–KOH were evaluated by electrochemical impedance spectroscopy (EIS) at open circuit potential with an applied 10 mV AC potential from 100 kHz to 10 mHz using a potentiostat/galvanostat (Autolab PGSTAT302N).

Mechanical properties of the gels were measured using a tensile tester (Instron 5943) at a rate of 10 mm $min^{-1}$ until failure (Figure S3). The force and initial cross-sectional area of the samples were used to calculate engineering stress, and the displacement and initial length were used to obtain engineering strain. Ultimate tensile strength was calculated from $\sigma_{UTS} = \frac{F_{max}}{A_o}$ while elongation at break was calculated from $EL\% = \frac{\Delta L}{L_o}$, where $F_{max}$, $A_o$, $\Delta L$ and $L_o$ are the maximum force, initial area, the change in length and original length of the samples, respectively. Young's modulus was calculated from the slope within the linear strain region.

A 90° peel test was conducted to determine the peel strength between the fabricated PAA–KOH and the GDL substrate using the Instron 5943. PAA–KOH on GDL was secured to a platform and then a Canon Type E transparency film was placed on top by pressing with the index finger. The transparency film was attached to a set of upper clamps and was peeled mechanically from the GDL at a speed of 50 mm $min^{-1}$ (Figure S4). The peel strength (mN $mm^{-1}$) was calculated by dividing the average load (mN) of the peel test by the width of the bonded pad (10 mm). Comparing the GDL and transparency film, PAA was stickier on the transparency film, allowing for the measurement of the adhesion strength of PAA on GDL.

The weight fraction of KOH was determined by the ratio of 6 M KOH mass equivalent in the medium that contributed to the ionic conductivity over the total mass of the PAA–KOH gel. The volume fraction of AA was determined by the ratio of volume of AA added over the total volume of PAA–KOH gel.

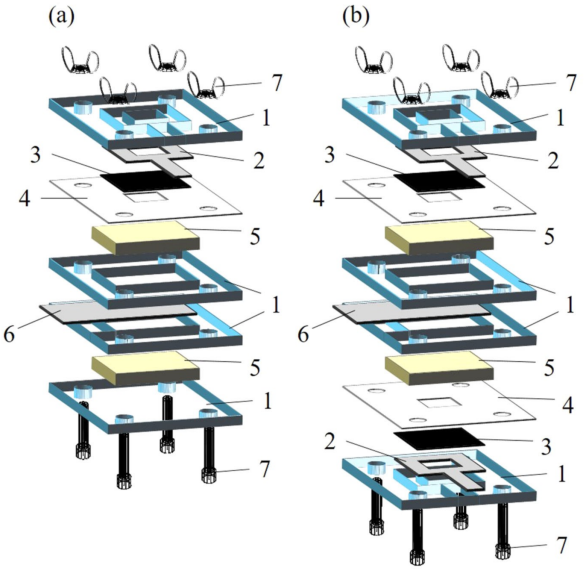


**Figure 1.** Homemade cell assembly for bi-electrode ZABs. a) Single air electrode (SAE) and b) double air electrode (DAE) designs. 1) Acrylic sheets, 2) Ni current collector, 3) GDL impregnated with $(Co,Fe)_3O_4$ decorated N-CNTs, 4) polypropylene film, 5) PAA–KOH, 6) Zn, 7) bolts and nuts.

### Battery testing

Before and after cycling, EIS measurements were performed with 10 mV AC potential from 100 kHz to 10 mHz at 1.2 V vs. $Zn/Zn^{2+}$ to reveal bulk, interfacial and charge transfer resistance. For rate testing, battery potential was measured by a galvanostatic method at a series of current densities of 2, 5, 10 and 20 mA $cm^{-2}$ for 5 min each with cut-off voltages of 0.6 V (discharge) and 2.5 V (charge), unless specified otherwise.

The time for charging a fresh ZAB with 0.25 M of ZnO in the PAA–KOH gels at 20 mA $cm^{-2}$ was determined as ~2 h from $I = \frac{zFN}{t}$, where I is applied current (A), z is number of electrons transferred, N is amount of ZnO (mol), F is the Faraday constant and t is charging time (s).

Cycling tests were also done through a galvanostatic method, with 30 min per cycle, using another potentiostat/galvanostat (Biologic VSP-300). The battery was discharged and charged at 10 or 20 mA $cm^{-2}$ for 10 min and the circuit was kept open for 5 min between steps. The purpose for the rest period between cycling steps was to allow the battery to stabilize and cool. Blurton et al. found that heat generation during cycling can facilitate self-discharge and water evaporation.[39] The discharge-charge efficiency was calculated by dividing the lowest discharge potential by the highest charge potential during the second cycle and the last cycle. The depth of discharge was calculated as the ratio of the discharge capacity over the total capacity of the battery at the specific current density and was determined to be ~1.8%.

Specific capacity was calculated from the galvanostatic discharge and normalized to the mass of consumed Zn from $C = \frac{It}{m \times 3600}$, where C is specific capacity (mAh $g_{Zn}^{-1}$), I is discharge current (mA), t is discharge time (s) and m is the mass of consumed Zn (g).

## 2. Results and Discussion

### 2.1. Evaluation of PAA–KOH Gel Electrolytes

The conductivity of an alkaline solution with a concentration of 6 to 6.5 M KOH reaches a maximum value of ~650 mS $cm^{-1}$ at room temperature (Figure 2a). At higher concentrations, the conductivity decreases because excess charge carriers ($K^+$ and $OH^-$) increase solution viscosity and resistivity. These values are also in agreement with literature data.[40–42] The conductivities of alkaline solutions containing AA monomers are reduced; e.g., the highest values are 608, 571, 501, 438 and 383 mS $cm^{-1}$ for solutions containing 0.25, 0.5, 1, 1.5 and 2 M AA,

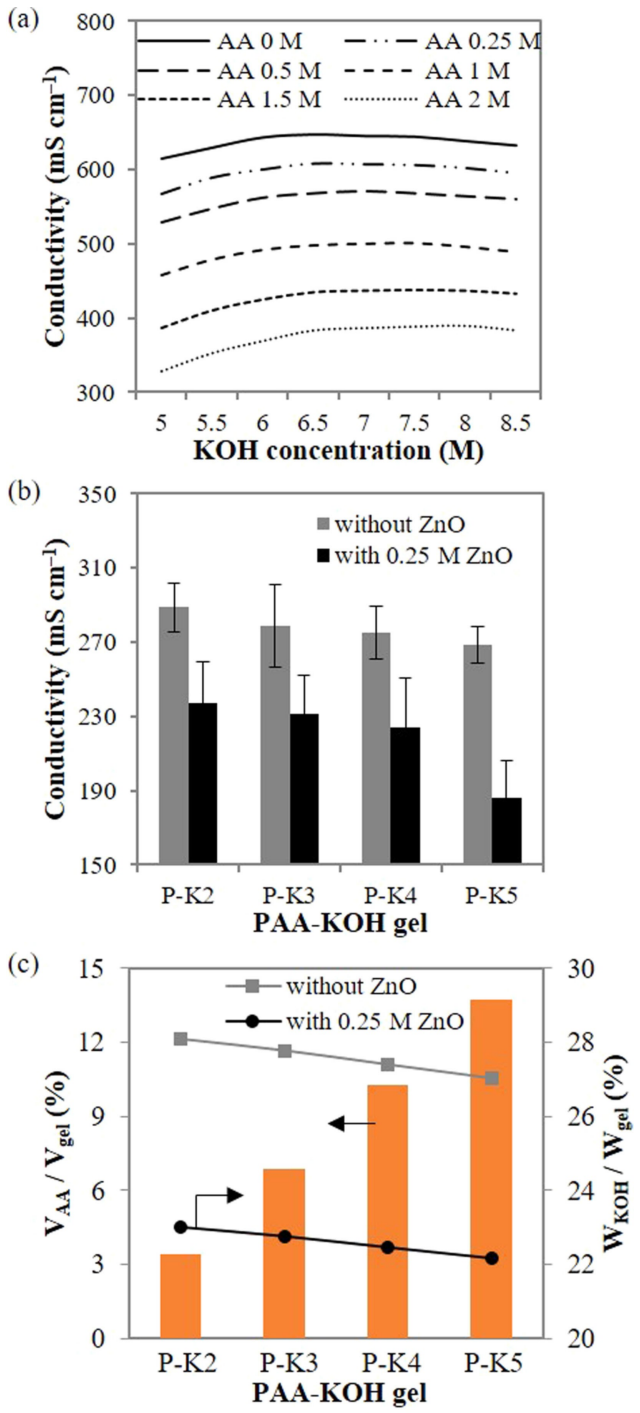


**Figure 2.** Evaluation of PAA–KOH. a) Conductivity of aqueous electrolytes, with different amounts of AA monomer, as a function of KOH concentration. b) Conductivity of PAA–KOH, with and without ZnO, as a function of PAA concentration. c) Mass ratio of 6 M KOH and volume ratio of AA contained within the PAA–KOH gels.

respectively. The peak conductivities are also shifted towards higher concentrations of KOH; e.g., the highest conductivity of an electrolyte with 2 M AA is obtained at 8 M KOH, which can be ascribed to compensation of charge carriers between the hydroxyl ions and carboxyl groups of AA monomers. Understanding this offset effect is important to achieve a GPE with a high conductivity, which is vital in obtaining high battery performance.

As shown in Figure 2b, the conductivities of all PAA–KOH gels are significantly reduced to ~280 mS cm$^{-1}$. This can be readily understood by the conductivity equation, $\sigma = Nze\mu$, where $\sigma$ is the ionic conductivity, N is number of ions (anions or cations) present per unit volume, z is the valence of the ion, e is the electron charge and $\mu$ is the mobility of the ions.[43] Upon polymerization, the presence of a polymeric network decreases both the N and $\mu$ values, leading to a decrease in $\sigma$. Here, the decrease in N is due to the volume fraction occupied by the immobile polymer network and the decrease in $\mu$ can be explained by the reduced apparent mobility of $K^+$ and $OH^-$ ions by the presence of the polymer network.

Thermodynamic behavior of the ternary KOH–ZnO–$H_2O$ system was experimentally investigated by Dirkse in 1959. In an aqueous electrolyte, ZnO was found to be saturated at 0.5 M in 6 M KOH.[44] Several studies reported that ionic conductivities decreased with increasing amount of ZnO.[44–45] In agreement with the literature, the addition of 0.25 M ZnO reduces the ionic conductivity of PAA–KOH gels; e.g., the conductivities of P–K2 and P–K5 gels decrease to 237 and 186 mS cm$^{-1}$, corresponding to a reduction of 15 to 30% of the initial conductivity, respectively. As shown in Figure 2c, P–K2 has a slightly higher weight fraction of KOH (28.1 vs 27 w/w%, respectively) and 4 times lower volume fraction of PAA than P–K5, while both have similar ionic conductivities of ~280 mS cm$^{-1}$. After adding 0.25 M ZnO, the volume of PAA in the gel remains unchanged; e.g., 3.4 vs 13.7 v/v% for P–K2 and P–K5, respectively. However, the weight fraction of KOH for all GPEs is further reduced at 5 w/w%. According to real-solution studies (without the polymeric host), all the 0.25 M ZnO appears to be $Zn(OH)_4^{2-}$ in a highly alkaline solution (~6.5 M KOH).[46] Although zincate ions are not the dominant charge carriers, they form tetrahedral structures with $OH^-$ ions, which results in a decrease in the net charge carrier ion concentration (N value of [$OH^-$]). The presence of the large ionic complex may also affect the overall mobility of the charge carrier ions. In addition, it can be postulated that a larger amount of PAA will lead to a smaller mesh size between polymeric networks that can effectively block large ions such as zincate ions. Previously, the authors found similar effects for PAA-based gels with varying concentrations of crosslinker.[38]

Although ZnO decreases the conductivity of PAA–KOH gels, it can help to reduce water activity and Zn corrosion.[47–49] Having zincate ions readily available in the electrolyte can also benefit the charging process.[36] OER rate testing was done for PAA–KOH gels with and without ZnO added (P–K2–ZnO and P–K2, respectively); the batteries were first discharged and then charged twice afterwards (Figure 3a). The charging curves for P–K2–ZnO exhibit essentially the same behavior. However, if no ZnO is added to the electrolyte (P–K2), the OER potential is only low at current densities of 2 and 5 mA cm$^{-2}$ for the first charging step and then becomes significantly larger at higher current densities, particularly for the second charging process. Since discharge is performed at all current densities before charging, the zincate ion formation reaction

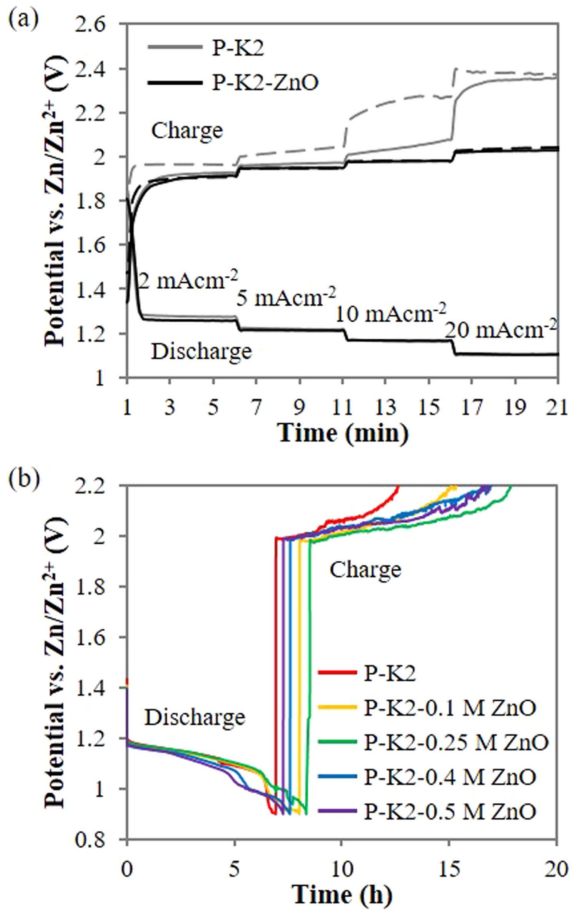


**Figure 3.** Electrochemical evaluation of PAA–KOH gels with various concentrations of ZnO. a) Rate test with the sequence discharge-charge-charge for ZABs using P–K2, with and without 0.25 M ZnO, at different current densities. Dashed lines represent the second charging cycle. b) Discharge-charge curves for ZABs using different concentrations of ZnO in P–K2 gels at a current density of 20 mA cm$^{-2}$.

($Zn + 4OH^- \rightarrow Zn(OH)_4^{2-} + 2e^-$) has already occurred and the zincate ion discharge product accumulates near the Zn electrode surface. The product is readily consumed during charging at current densities of 2 to 5 mA cm$^{-2}$. By the time a higher current density of 10 mA cm$^{-2}$ is reached, the zincate ions become depleted, so that a higher potential is required. Adding ZnO or $Zn(Ac)_2$ to the electrolyte ensures that the zincate ion concentration remains high enough to facilitate OER.

An attempt was made to compare the effects of the additives. Newly made batteries with different concentrations of ZnO or $Zn(Ac)_2$ were subjected to charging at 20 mA cm$^{-2}$ (Figure S5). Without any additives the ZAB reached the cut-off voltage virtually instantaneously. As the additive concentration is increased, the battery can maintain the charging potential for a longer period of time indicating that more zincate ions are available with a higher concentration of additives. In general, ZnO performs better as an additive than $Zn(Ac)_2$ in the gel electrolytes; as such, subsequent testing used only ZnO as an additive. An additive concentration of 0.5 M was the highest to be investigated since the gel became opaque (Figure S2). Increasing the zincate ion concentration in the vicinity of the Zn electrode surface can also result in faster passivation of the Zn electrode through the following reaction: $Zn(OH)_4^{2-} \rightarrow ZnO + H_2O + 2OH^-$.[50–51] Figure 3b shows the combined effects of discharging and different concentrations of ZnO added to GPEs on charging profiles at 20 mA cm$^{-2}$. For this experiment, cut-off voltages for discharge and charge were adjusted to 0.9 V and 2.2 V, respectively, because the thickening passive film could hamper the charging reaction. In other words, as the passive layer grows, there is less Zn active area for the charging reaction so that a high current density will require a higher voltage.[52–53] It can be seen that the discharging time is prolonged by 1.4 h with the addition of 0.25 M ZnO (discharging times of 6.9 h and 8.3 h for P–K2 and P–K2–0.25 M ZnO, respectively). Even with a supersaturated amount of ZnO, the battery can still last for 7.3 h (P–K2–0.5 M ZnO). For the charging process, batteries without ZnO can maintain charging for 5.7 h. The charging time increases to 7.2 h for 0.1 M ZnO and stabilizes at ~9.5 h for 0.25 to 0.5 M of ZnO. This result clearly shows that ZnO has positive effects on both discharging and charging for rechargeable ZABs, while an excessive amount of ZnO is not beneficial for discharging. The optimum amount of ZnO was determined to be 0.25 M and was used for all subsequent tests. All PAA–KOH gels are denoted as P–K–ZnO hereafter for simplicity.

Mechanical properties of hydrogels depend on the types and concentrations of crosslinking agents and polymeric monomers, as well as synthetic processes. Stress-strain and load-strain curves for as-prepared PAA–KOH gels are shown in Figure 4, while Young's moduli and peeling strengths calculated from Figures 4a and 4b, respectively, are listed in Table 2. In Figure 4a, tensile strength first increases and then decreases. Tensile strength is lowest at ~0.1 kPa for P–K2–ZnO and highest at 4.6 kPa for P–K4–ZnO. Since the concentration of AA monomers and the concentration of MBAA crosslinkers vary simultaneously, no particular trend is observed for tensile strength. However, the elongation at failure increases with increasing amount of AA. The elongation at failure increases from 0.7 to 9.7 mm/mm for P–K2–ZnO and P–K5–ZnO, respectively.

The tackiness of hydrogel electrolytes on GDL can be assessed by both the adhesive force and the corresponding displacement (Figure 4b). All samples showed mostly adhesive failure which means delamination at the interface, while cohesive failure is associated with tearing of the PAA–KOH

**Table 2.** Mechanical property parameters for PAA–KOH.

| Samples | P–K2–ZnO | P–K3–ZnO | P–K4–ZnO | P–K5–ZnO |
|---|---|---|---|---|
| Tensile strength [kPa] | 0.2 | 2.0 | 4.7 | 3.9 |
| Elongation [mm/mm] | 0.7 | 3.5 | 5.7 | 9.6 |
| Young's modulus [Pa] | 159.6 | 557.3 | 829.9 | 378.5 |
| Peeling strength [mN mm$^{-1}$] | 0.4 | 4.5 | 8.5 | 18 |
| Failure mode | Adhesive | Adhesive | Adhesive | Adhesive |

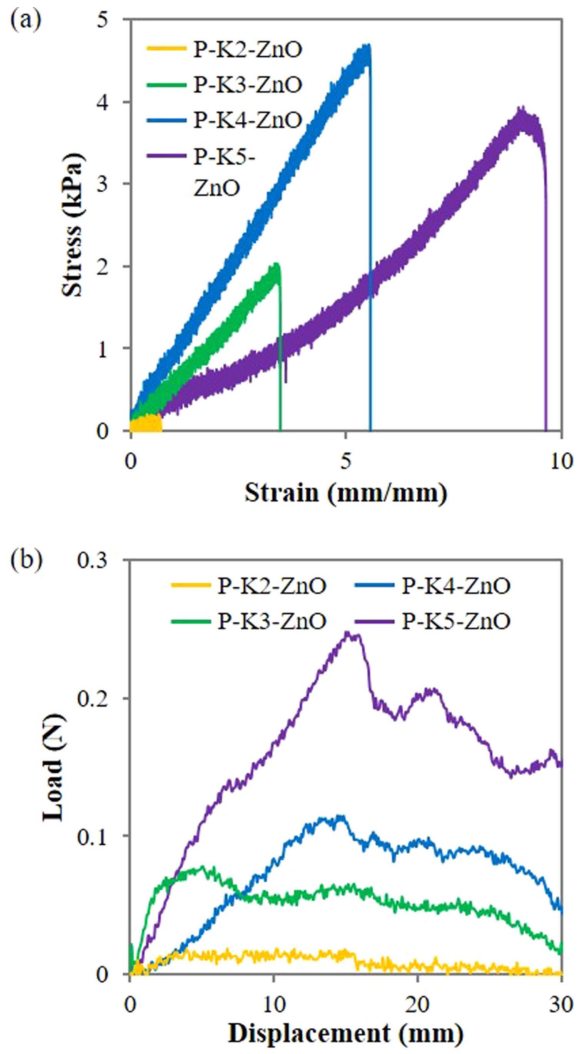


**Figure 4.** Mechanical properties of PAA–KOH gels. a) Tensile stress-strain curves at a rate of 10 mm miN$^{-1}$ and b) peeling strengths of PAA–KOH on GDL at a rate of 50 mm miN$^{-1}$.

gels.[54–55] In this study, the average force after the maximum detachment force is considered as a measure of adhesive force.[56] P–K2–ZnO has the lowest adhesive force of 0.004 N. Adhesive force increases drastically with higher concentration of AA; e.g., P–K3–ZnO, P–K4–ZnO and P–K5–ZnO have forces of 0.045, 0.085 and 0.18 N, respectively. Different peeling behaviors for these gel are also shown in Figure S4. The aim of the mechanical tests is to evaluate various characteristics related to the synthesis parameters and network formation of the weak hydrogel electrolytes and to propose how their properties may affect battery performance, which is further discussed in Section 2.2. More specifically, the hydrogel stiffness can affect the ability of ZABs to accommodate volume changes in the battery during discharge and charge processes, while the stickiness of gel electrolytes on GDL may be correlated to the efficiency in removing oxygen bubbles during the charging process.

### 2.2. Effects of PAA Matrix on Cycling Performance of ZABs

Benefiting from their solid-like nature, PAA–KOH electrolytes in ZABs can prevent the leaking and flooding issues that are associated with aqueous solutions. In Figure 5a, the discharge-charge rate tests show that PAA content in the network has a negligible effect on short-term battery performance. The efficiencies for each step were calculated by dividing the discharge potential by the charge potential. At current densities of 2, 5, 10 and 20 mA cm$^{-2}$, the discharge-charge efficiencies are respectively ~67, 62.4, 59.1 and 54.7 %. However, a high concentration of PAA does have a negative effect on depth of discharge (Figure 5b). At 20 mA cm$^{-2}$, the battery capacity is reduced from 163 to 127 mAh for P–K2–ZnO and P–K5–ZnO, respectively. This result is expected based on ionic conductivity measurements, as zincate ions cannot diffuse as easily in a denser polymer network.

To meet stringent criteria for the development of secondary ZABs, gel electrolytes also need to be able to accommodate volume changes and provide bubble management during cycling. It is well-known that during discharge the Zn electrode undergoes a volume expansion due to ZnO formation. Since the mass densities of Zn, $Zn(OH)_4^{2-}$ and ZnO are 7.14, 3.05 and 5.61 g cm$^{-3}$, respectively, a completely discharged Zn electrode may increase its active volume by approximately 27 %.[57] Such a pronounced change in volume leads to flooding of liquid electrolyte (for aqueous ZABs) through the large pores of the GDL.[58] In addition, interfacial interaction between the gel electrolyte and GDL plays a key role in bubble management. During charging, oxygen bubbles are produced $\left(2OH^- \rightarrow \frac{1}{2}O_2 + H_2O + 2e^-\right)$ and these bubbles can accumulate between the catalyst layer on the GDL and the electrolyte. In short, a volume increase can occur during discharging when Zn converts to ZnO, or from charging when $O_2$ bubbles cannot diffuse through the GDL. Elastic/plastic deformation of GPEs allows some room for volume changes of the battery.[59] In order to decouple the volume change caused by discharging, fresh batteries were used for charging tests. Overcharging curves are similar for all PAA compositions (Figure 5b). Interestingly, physical breakout through the GDL in batteries using P–K3–ZnO, P–K4–ZnO and P–K5–ZnO electrolytes was observed after 80, 52 and 78 min, respectively, as indicated by the arrows in Figure 5b, although the batteries still managed to function until the test ended. After the tests, the ZAB using P–K2–ZnO retains its original appearance, while the batteries with the other PAA–KOH gels exhibit breakthrough of the GDL (Figure 5c). Therefore, using GPEs that are sticky may backfire by allowing $O_2$ to quickly build up inside the battery. It should be noted that the ZAB with P–K4–ZnO had the earliest breakout although it is half as sticky as P–K5–ZnO and has the highest Young's modulus. It is speculated that stiffer GPEs do not accommodate deformation, thus the elevated pressure will push GDL outward sooner.

The electrical resistance of the ZABs was further investigated at 1.2 V before and after cycling at 20 mA cm$^{-2}$ (Figure 5d). The results are shown in Figure S6 and Table S2. In general, the total resistance of the as prepared or fresh

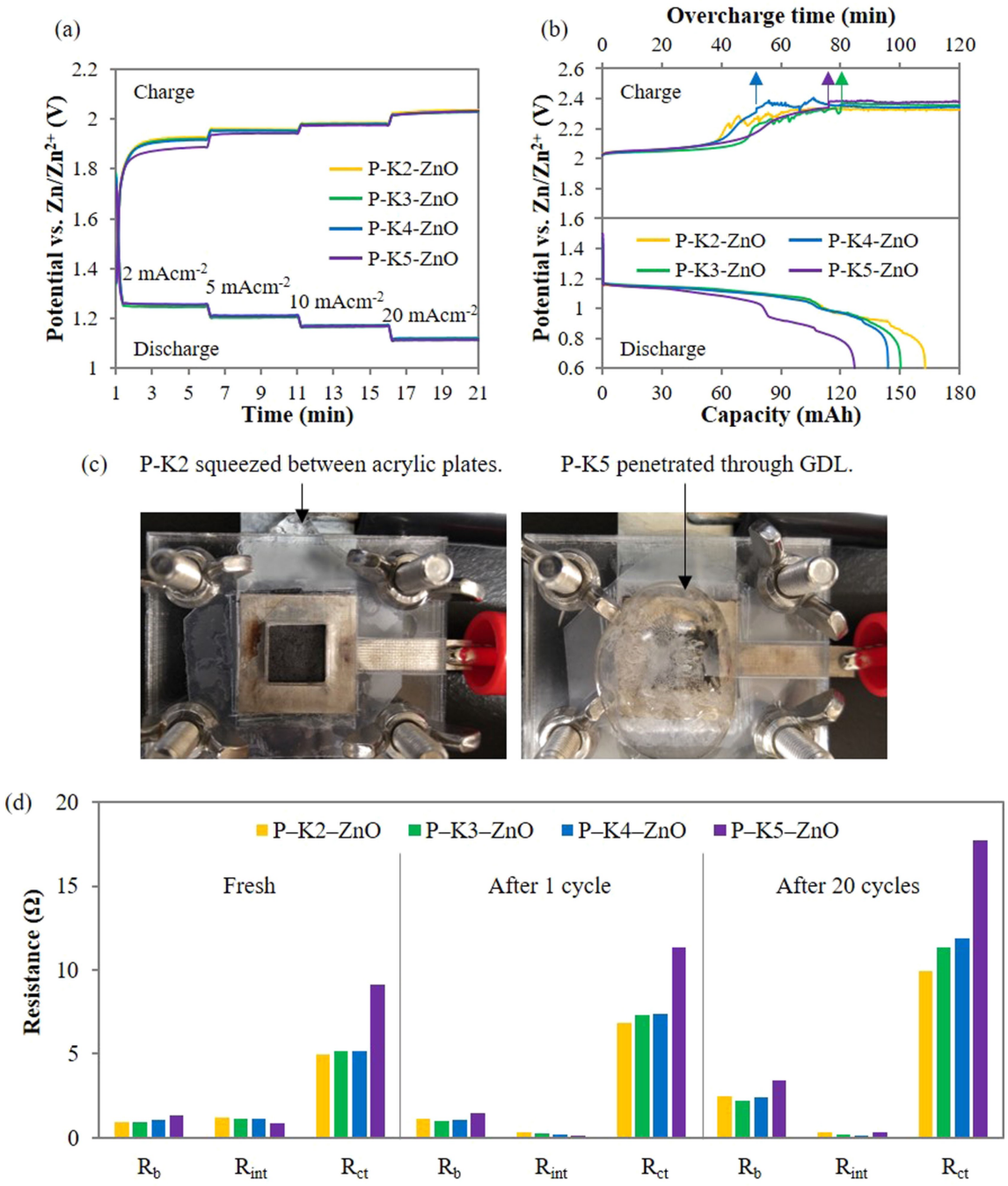


**Figure 5.** Evaluation of ZABs using PAA–KOH with various PAA concentrations. a) Discharge-charge rate curves. b) Full discharge and overcharge performance at 20 mA cm$^{-2}$. Arrows indicate the moment PAA–KOH protruded through and fractured the GDL. (c) Photographs showing the appearance of ZAB cells after charging. P–K2–ZnO squeezed between the acrylic plates and P–K5–ZnO penetrated through the GDL. (d) Electrical resistance for ZABs at 1.2 V before and after cycling at 20 mA cm$^{-2}$.

batteries (9–11 Ω) increases after 20 cycles (13–22 Ω) due to a variety of reasons including water evaporation, bifunctional catalyst degradation, Zn electrode passivation and oxygen bubble coalescence in the polymer network. The bulk resistance ($R_b$) is 0.9–1.3 Ω for as prepared batteries and increases to 2–3.5 Ω after 20 cycles. The resistance increase of the PAA-based electrolytes may be due to the formation of a froth layer that adheres to the air electrode surface during charging.[60] There is an obvious decrease in the interfacial resistance ($R_{int}$), which is considered to be the adsorption resistance of the gas species (oxygen in this case) on the air electrode.[61] After cycling, the hydrophobic pores of the air electrode enhance wettability and provide more area for gas adsorption and diffusion. $R_{int}$ also contributes the least to the overall battery resistance ($<0.3$ Ω after 20 cycles). The charge transfer resistance ($R_{ct}$) is considered to be affected by both the electrocatalytic activity of the catalysts under a fixed applied voltage and the accessible area of active sites.[62] At 1.2 V,

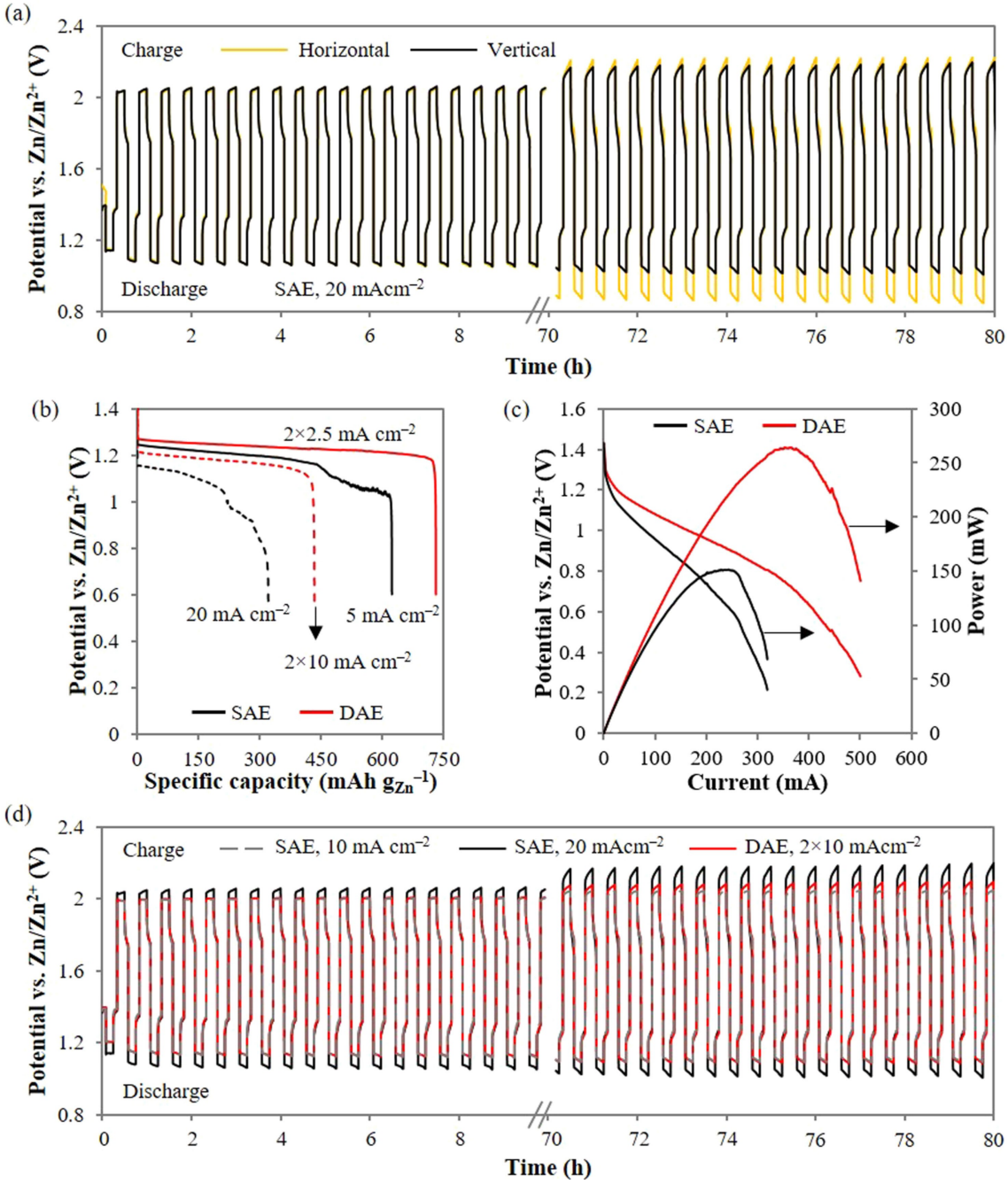


**Figure 6.** a) Cycling performance at 20 mA cm$^{-2}$ for ZABs with vertical and horizontal orientations. b–d) Comparison of ZABs using P–K2–ZnO electrolyte with two battery designs: b) full discharge curves at 5 and 20 mA; c) polarization and power curves, and d) cycling performance of ZABs at 10 and 20 mA cm$^{-2}$ using the SAE design and at 2×10 mA cm$^{-2}$ using the DAE design.

oxygen from the air and water from the electrolyte are consumed to produce hydroxyl ions ($O_2 + 2H_2O + 4e^- \rightarrow 4OH^-$). $R_{ct}$ for P–K5–ZnO is significantly higher than that of other gel electrolytes in the as prepared batteries, because of the reduction in mobility and activity of water in the denser hydrophilic polymer network. After cycling, batteries using P–K2–ZnO retained the lowest $R_{ct}$ values. This could be due to the influence of the bubble layer that forms between the air electrode and GPEs, which can obstruct the path for $H_2O$ transport to the electrode surface. In order to protect the integrity of ZABs and allow the reverse diffusion of oxygen, P–K2–ZnO was chosen for subsequent cycling tests.

### 2.3. Effect of Battery Design on ZAB Performance

For aqueous electrolytes, a horizontal battery configuration is favored over a vertical configuration since it allows for more evenly distributed Zn deposition by reducing dendrite growth and electrode deformation.[63] For GPEs, a vertical framework

**Table 3.** Comparison of ZAB cycling performance and maximum power density for this work and the recent literature.[a]

| Bifunctional catalysts | Electrolyte | Current density [mA cm$^{-2}$] | Cycle number | Initial – final efficiency [%] | Specific energy [Wh kg$_{Zn}^{-1}$] | Power density [mW cm$^{-2}$] | Ref. |
|---|---|---|---|---|---|---|---|
| $(Co,Fe)_3O_4$/N-CNT | 0.5 M PAA, 6.5 M KOH, 0.25 M ZnO, SAE design | 20 | 160 (30 min/cycle) | 54.7–47.5 | 748 @ 5 mA cm$^{-2}$ | 146 | This work |
| $(Co,Fe)_3O_4$/N-CNT | 0.5 M PAA, 6.5 M KOH, 0.25 M ZnO, DAE design | 2×10 | 160 (30 min/cycle) | 60.8–52.6 | 913 @ 5 mA cm$^{-2}$ | 2×135 | This work |
| $(Co,Fe)_3O_4$/N-CNT | 6 M KOH, 0.25 M ZnO | 20 | 200 (30 min/cycle) | 59.7–53.5 | N/A | 158 | [37] |
| $[Fe(CN)6]^{3-}$@(ZIF-8) | 6 M KOH, 0.2 M $Zn(Ac)_2$ | 5 | 120 (5 min/cycle) | 57.9–57.9 | 927.9 @ 5 mA cm$^{-2}$ | 22.2 | [64] |
| NPSC–$Co_2Fe_1$ | 6 M KOH, 0.2 M $Zn(Ac)_2$ | 10 | 150 (20 min/cycle) | 58.7–55 | N/A | 174.6 | [65] |
| NP–$Co_3O_4$/CC | 6 M KOH | 5 | 1200 (20 min/cycle) | 63.5–54.5 | N/A | 200 | [66] |
| $Co_3O_4$@N-CNMAs/CC | 10 w/v% PVA, 9 M KOH | 1 | 24 (20 min/cycle) | 67–60 | 1010 @ 1 mA cm$^{-2}$ | 65 | [67] |
| SilkNC/KB | 2.5 w/v% PVA, 7 M KOH. 0.1 M $Zn(Ac)_2$ | 1 | 30 (20 min/cycle) | 47.8–47.8 | N/A | 32.3 | [68] |
| $MnO_2$/$NRGO_{-Urea}$ | 3 g polyacrylamide, 20 wt% KOH | 5 | 140 (10 min/cycle) | 64.9–56 | 850 @ 10 mA cm$^{-2}$ | 105 | [69] |
| $LaMnO_3$ | 1.1 M PAA, 8.6 M KOH | 5 | 100 (10 min/cycle) | 64–57.5 | 730 @ 10 mA cm$^{-2}$ | 52.9 | [70] |
| CoPS | 7 wt% PAA–K, 6 M KOH, 0.2 M $Zn(Ac)_2$ | 5 | 150 (10 min/cycle) | 60–52.5 | 891 @ 10 mA cm$^{-2}$ | N/A | [71] |
| Fe–N–C/2D porous carbon | PANa-cellulose, 6 M KOH, 0.2 M $Zn(Ac)_2$ | 5 | 660 (10 min/cycle) | 59–58 | 930 @ 5 mA cm$^{-2}$ | 108.6 | [9] |

[a] ZIF-8: zeolitic imidazolate framework-8; NPSC–$Co_2Fe_1$: multi-doped nanoporous carbon; NP–$Co_3O_4$/CC: N-doped cobalt oxide on carbon cloth; $Co_3O_4$@N-CNMAs/CC: N-doped carbon nano-micro arrays on flexible carbon cloth; SilkNC/KB: silk-derived defect-rich and N-doped nanocarbon electrocatalyst/Ketjenblack, $MnO_2$/$NRGO_{-Urea}$ manganese dioxide nanowires supported on N-doped reduced graphene oxide; CoPS: cobalt phosphosulfide on carbon cloth, PAA–K: potassium salt-based poly(acrylic acid), PANa-cellulose: dual-network hydrogel electrolyte-based sodium polyacrylate (PANa) and cellulose.[64–65]

can be used to take advantage of gravity effects to facilitate the removal of oxygen bubbles. Both horizontal and vertical ZABs were cycled at 20 mA cm$^{-2}$. As shown in Figure 6a, the charge/discharge performance of horizontal and vertical cells is essentially the same at the beginning; however, after 23 h (~45 cycles) the vertical cell starts to show better efficiency. At the 160$^{th}$ cycle (80 h), the efficiencies are 38.8% and 47.5% for the horizontal and vertical configurations, respectively.

Tri-electrode battery designs, where ORR and OER occur on separate electrodes, have been proposed and tested as a means of improving air electrode efficiency. Tri-electrode designs, however, add more complexity to the battery and reduce its specific energy as a result of the extra mass from the additional electrode. The necessity for tri-electrode batteries has been mitigated somewhat by recent improvements in the energy efficiency of bifunctional catalysts.[9,64–71] A variation on the tri-electrode concept can be implemented by combining the benefits of a bifunctional catalyst and the solid state nature of gel electrolytes to double the area of the air electrode, thereby reducing its effective current density. In fact, this is a basic unit cell of the monopolar stack battery which was discussed by Muller et al in 1995.[72] As a proof-of-concept, two cell designs in a vertical configuration were utilized, one with a single air electrode (SAE) and one with a double air electrode (DAE); details are provided in the Experimental Section (cell fabrication). At a current of 2×2.5 mA cm$^{-2}$ (Figure 6b), the DAE can deliver a capacity of 730 mAh g$_{Zn}^{-1}$ which exceeds the capacity of the SAE design (623 mAh g$_{Zn}^{-1}$, at 5 mA cm$^{-2}$), contributing to a high specific energy of 913 Wh kg$_{Zn}^{-1}$. It should be noted that the specific capacity depends on discharge rate. As the current increases to 20 mA, the capacity of the DAE design decreases to 55%, while that of the SAE design drops to 46%. Figure 6c shows the power-current curves for ZABs. Since the maximum power is similar for the SAE and DAE designs (146 and 135 mW cm$^{-2}$, respectively), the final power obtained from the DAE is almost twice as high as that of SAE. The power output is superior to previously reported rechargeable ZABs (Table 3), including those using alkaline solutions as electrolytes. Capacity, energy density and power density of the as-assembled batteries, based on battery mass and volume, are provided in Table S3.

The DAE design also exhibits excellent cycling performance at 20 mA; its initial efficiency is the same as that for the SAE operating at 10 mA cm$^{-2}$ (Figure 6d). The final efficiency for ZABs using the SAE design is 53.9% at 10 mA cm$^{-2}$, while that using the DAE design is 52.6% at 2×10 mA cm$^{-2}$. The small amount of degradation at the end of cycling is believed to be caused by evaporation of water in the gels; however, the efficiency is still higher than a battery with a SAE design operating at the same current output (47.5% at 20 mA cm$^{-2}$). Table 3 shows a comparison of the battery performance between this work and the recent literature, for both aqueous and polymer electrolytes. A direct comparison can be made with reference,[37] as the same bifunctional catalysts were used in both studies. The efficiencies of ZABs using gel electrolytes are comparable with aqueous electrolytes at current densities

of 20 mA cm$^{-2}$. With proper cell design, gel electrolytes are a potential alternative to aqueous electrolytes, offering stable cyclability (190 cycles, equivalent to 95 h at 2×10 mA cm$^{-2}$ – Figure S7) and higher specific power with no leaking issues.

## 3. Conclusions

Various compositions of poly(acrylic acid) (PAA) were evaluated as the host material for an alkaline electrolyte in Zn-air batteries (ZABs). The effects of different gel electrolyte additives on the performance of a ZAB system were also evaluated. The addition of ZnO aided the charging process and reduced corrosion of the Zn electrode. The optimum concentration of ZnO was 0.25 M in PAA–KOH gels, which is lower than the saturation concentration that has been reported for aqueous, alkaline electrolytes. PAA stiffness and adhesion of the PAA matrix to the air electrode also affected battery performance. The lowest amount of monomer studied (0.5 M of AA) along with the highest amount of crosslinker (30 mM of MBAA) were the most suitable precursors for the fabricated PAA network, since this material was able to adapt to volume changes in the battery and facilitate the release of oxygen bubbles during charging.

A double air electrode (DAE) battery design was developed and compared with a conventional single air electrode (SAE) battery. The DAE, incorporated in a ZAB with a PAA–KOH electrolyte, had a high specific energy (913 Wh $kg_{Zn}^{-1}$), excellent cycling stability (at least 160 cycles at 2×10 mA cm$^{-2}$) and high power density output (2×135 mW cm$^{-2}$). This study opens up new horizons for battery design to take advantage of solid state electrolytes and optimize the performance of ZABs.

## *Acknowledgements*

*This work was supported by Future Energy Systems (FES T06 P03). The authors are grateful to Professor Anastasia Elias for access to the Instron 5943 tester.*

## *Conflict of Interest*

The authors declare no conflict of interest.

**Keywords:** poly(acrylic acid) · N,N′-methylenebis(acrylamide) · stiffness · adhesion · bubble management

[1] J. Fu, Z. P. Cano, M. G. Park, A. Yu, M. Fowler, Z. Chen, *Adv. Mater.* **2017**, *29*, 1604685.
[2] X. Cheng, J. Pan, Y. Zhao, M. Liao, H. Peng, *Adv. Energy Mater.* **2018**, *8*, 1702184.
[3] M. Liao, J. Wang, L. Ye, H. Sun, Y. Wen, C. Wang, X. Sun, B. Wang, H. Peng, *Angew. Chem. Int. Ed.* **2020**, *59*, 2273–2278.
[4] Z. Wang, X. Meng, Z. Wu, S. Mitra, *J. Energy Chem.* **2017**, *26*, 129–138.
[5] H. Peng, Y. Xu, J. Pan, Y. Zhao, L. Wang, X. Shi in *Flexible Metal-Air Batteries*, (Ed. X. b. Zhang), **2018**, pp. 367–396.
[6] S. Yang, K. Kim, *J. Electrochem. Sci. Technol.* **2018**, *9*, 339–344.
[7] O. Kwon, H. J. Hwang, Y. Ji, O. S. Jeon, J. P. Kim, C. Lee, Y. G. Shul, *Sci. Rep.* **2019**, *9*, 3175.
[8] X. Fan, J. Liu, J. Ding, Y. Deng, X. Han, W. Hu, C. Zhong, *Front. Chem.* **2019**, *7*.
[9] L. Ma, S. Chen, D. Wang, Q. Yang, F. Mo, G. Liang, N. Li, H. Zhang, J. A. Zapien, C. Zhi, *Adv. Energy Mater.* **2019**, *9*, 1803046.
[10] A. Poosapati, E. Jang, D. Madan, N. Jang, L. Hu, Y. Lan, *MRS Commun.* **2019**, *9*, 122–128.
[11] G. M. Wu, S. J. Lin, C. C. Yang, *J. Membr. Sci.* **2006**, *280*, 802–808.
[12] C.-C. Yang, S.-J. Lin, *J. Power Sources* **2002**, *112*, 497–503.
[13] C.-C. Yang, S.-J. Lin, S.-T. Hsu, *J. Power Sources* **2003**, *122*, 210–218.
[14] G.-M. Wu, S.-J. Lin, C.-C. Yang, *J. Membr. Sci.* **2006**, *275*, 127–133.
[15] J. Fu, D. U. Lee, F. M. Hassan, L. Yang, Z. Bai, M. G. Park, Z. Chen, *Adv. Mater.* **2015**, *27*, 5617–5622.
[16] Y. Xu, Y. Zhang, Z. Guo, J. Ren, Y. Wang, H. Peng, *Angew. Chem. Int. Ed. Engl.* **2015**, *54*, 15390–15394.
[17] T. N. T. Tran, H.-J. Chung, D. G. Ivey, *Electrochim. Acta* **2019**, *327*, 135021.
[18] C. Guan, A. Sumboja, H. Wu, W. Ren, X. Liu, H. Zhang, Z. Liu, C. Cheng, S. J. Pennycook, J. Wang, *Adv. Mater.* **2017**, *29*, 1704117.
[19] W. Zang, A. Sumboja, Y. Ma, H. Zhang, Y. Wu, S. Wu, H. Wu, Z. Liu, C. Guan, J. Wang, S. J. Pennycook, *ACS Catal.* **2018**, *8*, 8961–8969.
[20] C. Guan, A. Sumboja, W. Zang, Y. Qian, H. Zhang, X. Liu, Z. Liu, D. Zhao, S. J. Pennycook, J. Wang, *Energy Storage Mater.* **2019**, *16*, 243–250.
[21] Z. Zhang, C. Zuo, Z. Liu, Y. Yu, Y. Zuo, Y. Song, *J. Power Sources* **2014**, *251*, 470–475.
[22] L. Bockstie, D. Trevethan, S. Zaromb, *J. Electrochem. Soc.* **1963**, *110*, 267.
[23] R. S. M. Patnaik, S. Ganesh, G. Ashok, M. Ganesan, V. Kapali, *J. Power Sources* **1994**, *50*, 331–342.
[24] D.-J. Park, W.-G. Yang, H.-W. Jeong, K.-S. Ryu, *Bull. Korean Chem. Soc.* **2017**, *38*, 706–710.
[25] S. Müller, F. Holzer, O. Haas, *J. Appl. Electrochem.* **1998**, *28*, 895–898.
[26] J. Yu, H. Yang, X. Ai, X. Zhu, *J. Power Sources* **2001**, *103*, 93–97.
[27] S. Wang, Z. Yang, L. Zeng, *J. Electrochem. Soc.* **2009**, *156*, A18–A21.
[28] P. Bonnick, J. R. Dahn, *J. Electrochem. Soc.* **2012**, *159*, A981–A989.
[29] J. Huang, Z. Yang, R. Wang, Z. Zhang, Z. Feng, X. Xie, *J. Mater. Chem. A* **2015**, *3*, 7429–7436.
[30] A. M. Gaikwad, G. L. Whiting, D. A. Steingart, A. C. Arias, *Adv. Mater.* **2011**, *23*, 3251–3255.
[31] B. Zhu, X. Wang, P. Yao, J. Li, J. Zhu, *Chem. Sci.* **2019**, *10*, 7132–7148.
[32] C. Iclodean, B. Varga, N. Burnete, D. Cimerdean, B. Jurchiş, *IOP Conf. Ser.: Mater. Sci. Eng.* **2017**, *252*, 012058.
[33] Goals for Advanced High-Performance Batteries for Electric Vehicle (EV) Applications; https://www.uscar.org/guest/article_view.php?articles_id=85
[34] V. Caramia, B. Bozzini, *J. Renew. Sustain. Ener.* **2014**, *3*, 28.
[35] S. B. Sherman, Z. P. Cano, M. Fowler, Z. Chen, *AIMS Energy* **2018**, *6*, 121–145.
[36] T. N. T. Tran, M. Xiong, M. P. Clark, H. J. Chung, D. G. Ivey, *Electrochim. Acta* **2020** (submitted).
[37] D. Aasen, M. P. Clark, D. G. Ivey, *Batteries Supercaps* **2020**, *3*, 174–184.
[38] T. N. T. Tran, M. P. Clark, H. J. Chung, D. G. Ivey, *Batteries Supercaps* **2020**, 3, 409–416.
[39] K. F. Blurton, A. F. Sammells, *J. Power Sources* **1979**, *4*, 263–279.
[40] R. J. Guanti, P. J. Moran, *J. Appl. Electrochem.* **1986**, *16*, 678–682.
[41] D. M. See, R. E. White, *J. Chem. Eng. Data* **1997**, *42*, 1266–1268.
[42] X. Zhu, H. Yang, Y. Cao, X. Ai, *Electrochim. Acta* **2004**, *49*, 2533–2539.
[43] P. Atkins, J. De Paula, J. Keeler, *Atkins' Physical Chemistry*, Oxford University Press, **2018**, p. 908.
[44] T. P. Dirkse, *J. Electrochem. Soc.* **1959**, *106*, 154–155.
[45] W. H. Dyson, L. A. Schreier, W. P. Sholette, A. J. Salkind, *J. Electrochem. Soc.* **1968**, *115*, 566.
[46] A. Anderko, J. W. Berthold, M. Rafal, S. J. Sanders in *Application of aqueous simulation software to battery research, Vol. 95* Eds.: A. J. Salkind, F. McLarnon, V. S. Bagotskii), The Electrochemical Society, Pennington, NJ, **1996**, p. 262.
[47] R. Shivkumar, G. Paruthimal Kalaignan, T. Vasudevan, *J. Power Sources* **1995**, *55*, 53–62.
[48] X. Y. Wang, J. M. Wang, Q. L. Wang, H. B. Shao, J. Q. Zhang, *Mater. Corros.* **2011**, *62*, 1149–1152.
[49] A. R. Mainar, O. Leonet, M. Bengoechea, I. Boyano, I. de Meatza, A. Kvasha, A. Guerfi, J. A. Blázquez, *Int. J. Energy Res.* **2016**, *40*, 1032–1049.
[50] M. Bockelmann, L. Reining, U. Kunz, T. Turek, *Electrochim. Acta* **2017**, *237*, 276–298.

[51] M. Bockelmann, M. Becker, L. Reining, U. Kunz, T. Turek, *J. Electrochem. Soc.* **2018**, *165*, A3048-A3055.
[52] J. Yi, P. Liang, X. Liu, K. Wu, Y. Liu, Y. Wang, Y. Xia, J. Zhang, *Energy Environ. Sci.* **2018**, *11*, 3075–3095.
[53] Z. Zhao, X. Fan, J. Ding, W. Hu, C. Zhong, J. Lu, *ACS Energy Lett.* **2019**, *4*, 2259–2270.
[54] M. V. Hoang, H.-J. Chung, A. L. Elias, *J. Micromech. Microeng.* **2016**, *26*, 105019.
[55] C. F. Chen, K. Wharton, *RSC Adv.* **2017**, *7*, 1286–1289.
[56] M. Horstmann, W. Müller, B. D. Asmussen in *Principles of Skin Adhesion and Methods For Measuring Adhesion of Transdermal Systems*, Eds.: E. Mathiowitz, D. E. Chickering-III, C.-M. Lehr), CRC Press, New York, **1999**, pp. 175–195.
[57] T. Arlt, D. Schröder, U. Krewer, I. Manke, *Phys. Chem. Chem. Phys.* **2014**, *16*, 22273–22280.
[58] D. Schröder, T. Arlt, U. Krewer, I. Manke, *Electrochem. Commun.* **2014**, *40*, 88–91.
[59] J. Fu in *Material Design and Engineering for Polymer Electrolyte Membrane Zinc-Air Batteries, Doctor of Philosophy* University of Waterloo, Waterloo, Ontario, Canada, **2018**, p. 147.
[60] D. Kiuchi, H. Matsushima, Y. Fukunaka, K. Kuribayashi, *J. Electrochem. Soc.* **2006**, *153*, E138–E143.
[61] M. Wang, Z. Wang, Z. Guo, *Int. J. Hydrogen Energy* **2009**, *34*, 5311–5317.
[62] C. N. Ho, B. J. Hwang, *J. Electroanal. Chem.* **1994**, *377*, 177–190.
[63] W. Hong, H. Li, B. Wang, *Int. J. Electrochem. Sci.* **2016**, *11*, 3843–3851.
[64] D. Chen, J. Ji, Z. Jiang, M. Ling, Z. Jiang, X. Peng, *J. Power Sources* **2020**, *450*, 227660.
[65] K. He, J. Zai, X. Liu, Y. Zhu, A. Iqbal, T. Tadesse Tsega, Y. Zhang, N. Ali, X. Qian, *Appl. Catal. B* **2020**, *265*, 118594.
[66] X. Wang, Z. Liao, Y. Fu, C. Neumann, A. Turchanin, G. Nam, E. Zschech, J. Cho, J. Zhang, X. Feng, *Energy Storage Mater.* **2020**, *26*, 157–164.
[67] Y. Zhong, Z. Pan, X. Wang, J. Yang, Y. Qiu, S. Xu, Y. Lu, Q. Huang, W. Li, *Adv. Sci.* **2019**, *6*, 1802243.
[68] C. Wang, N.-H. Xie, Y. Zhang, Z. Huang, K. Xia, H. Wang, S. Guo, B.-Q. Xu, Y. Zhang, *Chem. Mater.* **2019**, *31*, 1023–1029.
[69] H. Miao, B. Chen, S. Li, X. Wu, Q. Wang, C. Zhang, Z. Sun, H. Li, *J. Power Sources* **2020**, *450*, 227653.
[70] H. Miao, X. Wu, B. Chen, Q. Wang, F. Wang, J. Wang, C. Zhang, H. Zhang, J. Yuan, Q. Zhang, *Electrochim. Acta* **2020**, *333*, 135566.
[71] B. Roy, K. J. Shebin, S. Sampath, *J. Power Sources* **2020**, *450*, 227661.
[72] S. Mueller, F. Holzer, O. Haas, C. Schlatter, C. Comninellis, *Chimia* **1995**, *49*, 27–32.

Manuscript received: March 13, 2020
Revised manuscript received: May 3, 2020
Accepted manuscript online: May 4, 2020
Version of record online: May 19, 2020